Validation of experimental whole-body SAR assessment method in a complex indoor environment. — Source link ⬈

Aliou Bamba, Wout Joseph, Günter Vermeeren, Emmeric Tanghe ...+5 more authors

Institutions: Ghent University, university of lille, Aalborg University

Related papers:

- Guidelines for limiting exposure to time-varying electric, magnetic, and electromagnetic fields (up to 300 GHz)

- Room electromagnetics

- Reverberation and Absorption in an Aircraft Cabin With the Impact of Passengers

- Angular and Shadowing Characteristics of Dense Multipath Components in Indoor Radio Channels

- Experimental Assessment of Specific Absorption Rate Using Room Electromagnetics

Validation of Experimental whole-body SAR Assessment Method in a Complex Indoor Environment

Aliou Bamba[1,*], Wout Joseph[1], Gunter Vermeeren[1], Emmeric Tanghe[1], Davy P. Gaillot[2], Jørgen B. Andersen[3], Jesper Ødum Nielsen[3], Martine Lienard[2], and Luc Martens[1].

[1]Ghent University / IBBT, Department of Information Technology

Gaston Crommenlaan 8 box 201, B-9050 Ghent, Belgium

Fax: +32 9 33 14 899, Tel: +32 9 33 14 908

[*]Email: aliou.bamba@intec.ugent.be

[2]Group TELICE, IEMN, University of Lille, France

[3]APNet, Department of Electronic Systems

Faculty of Engineering and Science, Aalborg University, Denmark

Running title: Validation of Experimental whole-body SAR Assessment Method

Abstract

Assessing experimentally the whole-body specific absorption rate (SAR_{wb}) in a complex indoor environment is very challenging. An experimental method based on room electromagnetics theory (accounting only the Line-Of-Sight as specular path) to assess the whole-body SAR is validated by numerical simulations with the Finite-Difference Time-Domain method. Furthermore, the method accounts for the diffuse multipath components (DMC) in the total absorption rate by considering the reverberation time of the investigated room, which describes all the losses in a complex indoor environment. The advantage of the proposed method is that it allows discarding the computation burden because it does not use any discretizations. Results show good agreement between measurement and computation at 2.8 GHz, as long as the plane wave assumption is valid, i.e., for high distances from the transmitter. Relative deviations 0.71% and 4% have been obtained for far-field scenarios, and 77.5% for the near field-scenario. The contribution of the DMC in the total absorption rate is also quantified here, which has never been investigated earlier. It is found that the DMC may represent an important part of the total absorption rate; its contribution may reach up to 90% for certain scenarios in an indoor environment.

INTRODUCTION

The International Commission on Non-Ionizing Radiation Protection (ICNIRP) defines the Specific energy Absorption Rate (SAR) as a basic restriction for human exposure in the radio frequency (RF) band [ICNIRP, 1998]. Various works based on numerical computations such as the Finite-Difference Time-Domain (FDTD) method have assessed the SAR in phantoms [Dimbylow, 2002; Wang et al., 2006], but the whole-body SAR remains a difficult quantity to measure in any human body, especially in complex environments.

The whole-body SAR have been assessed in a human body model in a realistic electromagnetic environment [Vermeeren et al., 2008], however the results were obtained using a statistical incident field approach. The absorption of radio frequency (RF) electromagnetic fields (EMF) in the frequency range from 50 MHz to 2.5 GHz in an anatomically "correct" human body is investigated in Kühn et al. [2009], the simulations have been conducted for few incident fields directions while focusing more on the phantom anatomy. Joseph et al. [2010] calculates the whole-body SAR from measurements data obtained with personal exposure meters for different humans spheroid and frequencies. The authors investigated the absorption rate for different scenarios, among which the indoor environments. An interesting approach to assess the human absorption rate in a realistic urban environment can be found in Bernardi et al. [2003]. This method simulates a room with thin plates of materials having different properties, while the transmitter is located outside of the room. Because the propagation mechanism is so complex in an indoor environment, a uniform asymptotic theory of diffraction (UTD) technique is used to account for the fields resulting from scattering and diffraction. A geospatial model for RF-EMF prediction is introduced in Bürgi et al. [2010]. The RF-EMF has been adequately predicted for outdoor scenarios, but the indoor scenarios did not meet the same success because of the

considerable simplifications made for the investigated indoor environment, which is actually very complex, comprised of different parts (the interior walls, the floor, the ceiling, the furniture, and so on) with different material properties. Therefore, the propagation mechanisms in such environments must be well understood to faithfully assess the SAR_{wb}. Recent studies [Richter, 2005; Poutanen et al., 2011] have shown that wireless channels typically consist of a set of specular paths and diffuse multipath components (DMC) resulting from coherent and non-coherent reflections off scatterers present in the room, respectively. The DMC represents the part of the channel which cannot be characterized with specular paths. In other words, the DMC is the remainder of the measured power delay profile (PDP) after removing the contribution of all the specular paths. The characteristics of the DMC in an indoor environment were investigated in Poutanen et al. [2011], where it turns out that the contribution of the DMC to the total power may range from 10% to 95%.

Bamba et al. [2012] introduced a new experimental method to assess the whole-body SAR in a human in a realistic indoor environment. Although good agreement was obtained with results in literature, this is not sufficient to validate the proposed method because the humans were different, and the comparisons have been made with normalized power density.

The proposed method is based on the room electromagnetics theory [Andersen et al., 2007, 2012] which states the following: the total power in an indoor environment is comprised of the first specular path (i.e., the LOS component) and the DMC contribution. All the losses in a closed room can be described with a single parameter called the reverberation time (τ). The reverberation time is the decay rate of the diffuse power in an indoor environment. Bamba et al. [2012] also showed that the contribution of the DMC in the total power depends not only on the separation between the receiver and the transmitter but also on the reverberation time, which is a

characteristic of a room. The novelty of our method potentially relies in its ability to predict the

SAR_{wb} in an arbitrary complex indoor environment while accounting the actual power densities.

Although the absorption rate in a human will clearly be strongly dependent on the DMC, its

contribution to the SAR_{wb} is completely missing in the literature and must be carefully

addressed.

The objective of this paper is to experimentally assess the SAR_{wb} in a phantom from the

measured absorption cross section (ACS), i.e., the human or phantom surface illuminated in

diffuse fields and afterwards simulate the same phantom using a FDTD software, thus validating

the proposed method. Here, the SAR_{wb} dependency to the DMC is evaluated and discussed for

various scenarios. FDTD numerical calculations under the same propagation and phantom

conditions are performed to validate the experimental approach.

MATERIALS AND METHODS

Measurement equipment

A virtual Multiple-Input-Multiple-Output (MIMO) channel sounder is used to probe the channel.

A virtual channel sounder is a measurement system equipped with a single physical antenna at

each side, namely the transmitter (Tx) and the receiver (Rx), as shown in Figure 1. A network

analyzer (Rohde & Schwarz ZVR, Rohde &Schwarz, Munich, Germany) is used to measure the

complex channel frequency response for a set of transmitting and receiving antenna positions. As

transmitting and receiving antenna, broadband omnidirectional biconical antennas of type

Electro-Metrics EM-6116 (Electro-Metrics, New York City, NY, USA) are used. To be able to

perform measurements for large Tx-Rx separations, one port of the network analyzer is

connected to the Tx through an RF/optical link with an optical fiber of length 500 m. We

connected the optical fiber to the Tx side because the Tx carriage moves sometimes from a position to another one and the Rx carriage is fixed. The Rx carriage supports the measurement laptop, the network analyzer and other equipments, while the Tx carriage supports mainly the optical fiber rolls and other equipments. Additional supporting information about the measurement system can be found in the online version of this article: Figure 7 shows a picture of the carriages and the antennas (online supplementary materials). The signal generated by the network analyzer is sent into the Tx via the optical fiber. The RF signal sent into the Tx and the RF signal coming from the Rx are both amplified using a Nextec-RF NB00453 amplifier (Nextec Microwave & RF, Santa Clara, CA, USA) with an average gain of 37 dB.

The amplifiers assure that the signal-to-noise ratio at the receiving port of the network analyzer is at least 20 dB. The calibration of the network analyzer is done at the connectors of the Tx and Rx antenna, and include both the RF/optical link and the amplifiers. By means of stepper motors, the antennas are moved from one position to another one. Performing the measurements with several positions of the Tx and Rx antenna emulate thus a MIMO system (Fig. 1). The measurements were performed at 2.8 GHz within a bandwidth of 200 MHz, with a frequency resolution of 0.5 MHz (401 frequency points). This band is representative for the Wireless Local Area Network (WLAN) exposure at 2.4 GHz (2.8 GHz band is chosen instead of 2.4 GHz to avoid interference).

For the present work the Tx antenna is fixed in the array and the Rx antenna is positioned at 100 (10×10) different positions forming a virtual uniform rectangular array. Because of the small-scale fading, performing measurements with more positions of the antenna (in the virtual array)

ensures the Power-Delay-Profile (PDP) to be smooth enough after averaging. Both antennas are polarized vertically and positioned at a height of about 1.80 m above the ground.

Considered scenarios and simulation settings

As already stated, the contribution of the diffuse power density in the total power may vary drastically [Poutanen et al., 2011].

Five identical cylindrical phantoms (Ph1, Ph2, …, Ph5) in polyvinyl chloride (PVC) with an inner radius of 119.5 mm and an outer radius of 124.5 mm (thickness = 5 mm) and a height of 1500 mm have been used and filled with water. The phantoms are arbitrarily located in the room, more information about the location and the environment is shown in Figure 8 of the online version of this article (online supplementary materials). The PVC electrical properties at 2.8 GHz are as follows: conductivity = 0.003 Ω^{-1}/m and relative permittivity = 2.58. Dosimetric measurements are usually performed in phantoms containing liquid with dielectric properties similar to those of biological tissues, i.e., the tissue-equivalent liquid, to emulate the actual SAR in a human. Given that the purpose of our experiment focuses on the validation of a method rather than simulating the actual SAR values in a human tissue, i.e., comparison between experimental and numerical results, the cylinders can be filled with any liquid having dielectric properties that allow absorption. For the present work, water has been used to fill the phantoms, we measured its properties and the followings values have been obtained: $\sigma = 1.58 \, \Omega^{-1}$/m (conductivity), $\varepsilon_r = 77.32$ (relative permittivity). The dielectric properties of the liquid are measured using the Hewlett Packard HP85070A dielectric probe kit with the Hewlett Packard HP8753D network analyzer (Agilent Technologies, Santa Clara, CA, USA) [Joseph et al., 2005]. The liquid has a mass density $\rho = 1000$ kg/m^3. Figure 2 shows a scheme of the related phantom.

For the numerical simulation the following settings are used. The FDTD solver [Taflove et al,. 2005] is used to compute numerically the averaged whole-body SAR absorbed by a phantom. A harmonic excitation is used in the simulation. A rectangular plane wave source (the duration of the plane wave is set to 25 periods at 2.8 GHz) which is based on the Total-Field Scattered-Field (TFSF) technique [Merewether et al,. 1980]. The maximum grid step in the cylinder phantom equals $0.07\lambda_{ph}$, where λ_{ph} is the wavelength in the phantom. To avoid reflections of the waves impinging on the boundaries into the simulation domain, uniaxial perfectly match layer (UPML) is used as absorbing boundary conditions. The UPML has been set so that more than 95% of the power of incident waves will be absorbed by the boundary layers. Given the dimensions of the cylinder, we obtain a volume of about 0.068 m^3, which leads to a mass of 68 kg.

METHODOLOGY

The flow chart of the validation methodology is depicted in Figure 9 and available in the online version of this paper (online supplementary materials). We will now explain the different steps. In the following, all incident plane waves are assumed to be in the horizontal plane (Fig. 2), i.e., normal incidence. We assume a transmitted power of 1 W.

It is noteworthy to mention that we use five phantoms to assess the absorption cross section (ACS) of a phantom, i.e., the total surface of the phantom illuminated in a completely diffuse field. The ACS could be derived from only one phantom, however because of the measurement uncertainties, the results are more accurate if an averaging of the ACS is done over several phantoms (5 in our case, see further). Since the ACS of the phantom is derived, we do not need anymore the phantoms to assess the SAR$_{wb}$. We assess the SAR$_{wb}$ in a cylindrical phantom instead of actual humans because we focus more on the method validation rather than checking

the compliance with the ICNIRP reference levels, and because of the shape of the cylinder which eases the determination of the ratio between the ACS in diffuse fields, and the one induced by a single plane wave (see Equation (4)). Furthermore, it is difficult to have humans with similar body surface (in case we made the assumption that the persons have equal ACS for simplification sake in the measurements part).

Theory for experimental SAR assessment based on room electromagnetics

Basically, the experimental assessment of the whole-body SAR is comprised of two parts: the determination of the absorption cross section of the phantom and the determination of the incident power densities.

In a first step (Step 1 in Fig. 9), the measurements of the PDP are performed using the virtual channel sounder. The absorption cross section assessment methodology is based on room electromagnetics theory [Andersen et al., 2007], which states that all the losses in a closed room can be described with a single parameter, called the reverberation time. From the reverberation time τ, it is possible to assess the effective absorption area (A_n') as follows:

$$A_n' = \eta A_n = \frac{4V}{c\tau_n} \tag{1}$$

where η, A_n, V, c $= 3 \times 10^8$ m/s, and τ_n are the fraction of energy absorbed (by the area), the surface of the area absorbing electromagnetic radiation, the room volume, the velocity of light in vacuum, and the reverberation time when n phantom(s) are present in the room, respectively. The reverberation time is related to the slope in the PDP (the PDP plots the logarithmic power versus delay) decay as follows:

$$\tau = -\frac{10\log(e)}{slope} \tag{2}$$

where e = 2.718… is the *Euler's number* and *slope* is the slope of the linear tail in the PDP. The slope is derived by fitting the PDP tail (from its peak value to the noise level). The reverberation time assessment from the PDP is done in the Step 2 of Figure 9. Since the reverberation time is known, the related absorbing area in the room is easily computed using Equation (1). A PDP, the slope value, and the corresponding reverberation time value in the investigated room (volume $\approx$ 360 m^3) without phantoms are shown in Figure 3. For this example, we obtain from the *slope* of the PDP a value of τ = 52.7 ns.

We vary then the room occupation to obtain different absorbing area values as a function of the number of phantoms. Hence the absorption cross section is obtained by the determination of the slope of the linear regression of the points related to the different absorbing areas for the different number of phantoms. Figure 4 shows the determination of the ACS (for one time observation) in the considered environment by using 0, 1, …, 5 phantoms. Each point in this figure corresponds to the absorbing area of the room containing the corresponding number of phantom(s). For each set of the phantom(s) in the room, measurements M_1^i and M_2^i ($i \in \{0, …, 5\}$ is the number of phantoms) are performed, and 10 time observations have been recorded during each measurement. From the measurements M_j (j=1, 2 indicates that the measurements have been performed twice to ensure the repeatability), one absorption cross section is derived per time observation (see Figure 4). Eventually, we obtain 20 values of the absorption cross section of a phantom for the whole measurement campaign (Step 3 in Fig. 9). The entire procedure of assessing the reverberation time and the absorption cross section is detailed in Bamba et al. [2012].

In the fourth step, the experimental LOS component power density is investigated based on the Friis equation [Friis, 1946] and the diffuse power density has been addressed in Andersen et al. [2012]. The expression of the DMC power density is:

$$I_{dif} = \frac{P_0}{\pi \eta A} e^{-\frac{d_0}{c\tau}} . \eta_{pol} \tag{3}$$

where P_0, d_0, and η_{pol} are the transmitted power, the distance Tx-phantom, and the polarization factor in diffuse fields, respectively. The polarization factor is set to 0.5 because we assume complete depolarization. The results of both the LOS and the DMC power densities as a function of the separation from the Tx are shown in Figure 5. Three cases (indicated by ellipses in Fig. 5) are selected for the assessment of the whole-body SAR: in the vicinity of the transmitter where the LOS component power density is dominating (scenario 1), at the reverberation distance i.e., the distance where the LOS component and the DMC power densities are the same (scenario 2) and at last a location far away from the Tx where the DMC power density is dominating over the LOS component power density (scenario 3).

In step 5 of Figure 9, the ACS in diffuse fields i.e., ACS_{cyl}^{dif}, and the one derived from the LOS component illumination i.e., ACS_{cyl}^{los} are combined with the power densities to calculate the total whole-body absorption rate. For the calculation of the ACS due to the LOS component, not the same absorption cross section as for the DMC can be used since the LOS plane wave does not *see* the whole cylinder, but it rather *sees* the front view of the cylinder. Let us now derive the ACS for the incident LOS plane wave for the cylindrical phantom. The whole-absorption cross section of the cylinder ACS_{cyl}^{dif} was derived in complete diffuse fields from the measurements.

From Equation (1), it can be easily shown that $ACS_{cyl}^{dif} = \eta_{cyl} A_{cyl}$, where η_{cyl} and A_{cyl} are the ratio of power absorbed by the phantom and the incident power, and the total surface of the

phantom, respectively. Since the incoming LOS plane component *sees* only the front of the cylinder, the associated absorption cross section is expressed as $ACS_{cyl}^{los} = \eta_{cyl} A_{cyl}^{frontview}$.

Hence the ACS for diffuse and LOS cases are related as follows:

$$\frac{ACS_{cyl}^{dif}}{ACS_{cyl}^{los}} = \frac{\eta_{cyl} A_{cyl}}{\eta_{cyl} A_{cyl}^{frontview}} = \frac{\eta_{cyl} 2\pi rh}{\eta_{cyl} 2rh} = \pi \tag{4}$$

where r and h are the radius and the height of the cylindrical phantom, respectively (see Fig. 2). Obviously, this ratio will depend on the shape of the considered phantom, but it is easy to obtain it for any other geometrical shapes. For a human, further simulations are needed to derive the relation between the ACS illuminated in diffuse fields and the ACS resulting in a LOS component illumination for different azimuthal angles. Hence, the method can be applied for any posture of the exposed person since the absorption cross section (in diffuse fields) and the power densities assessment methods are independent of the human or phantom posture. Finally, the experimental measured whole-body SAR is derived:

$$\begin{aligned} SAR_{wb}^{exp} &= SAR_{wb}^{exp,spec} + SAR_{wb}^{exp,dmc} \\ &= \frac{ACS_{cyl}^{los} \times I_{spec}^{total}}{m} + \frac{ACS_{cyl}^{dif} \times I_{dif}}{m} \\ &= \frac{ACS_{cyl}^{dif} \times I_{spec}^{total}}{\pi m} + \frac{ACS_{cyl}^{dif} \times I_{dif}}{m} \\ &= \frac{ACS}{m}\left(I_{dif} + \frac{1}{\pi} \sum_{k=1}^{N_{spec}} I_{spec}^{k} \right) \end{aligned} \tag{5}$$

where $SAR_{wb}^{exp,spec}$, $SAR_{wb}^{exp,dmc}$, m, I_{dif}, I_{spec}^{k}, and N_{spec} represent the experimental absorption rate due to the specular components, the experimental absorption rate due to the DMC, the mass of the phantom in kg, the total power density of the DMC, the power density of the kth specular path, and the total number of specular paths, respectively. We introduce N_{spec} here to show that the method can be extended to several specular paths, however $N_{spec} = 1$ (only the LOS

component is considered [Andersen et al., 2012]) for the present experiment. In Equation (5), we assume that the total whole-body SAR SAR_{wb}^{exp} is the summation of the SAR induced by the LOS component and the one induced by the DMC.

Note that the reverberation time notion is only valid if there is complete diffuse fields. However, the complete diffuse field is mainly due to the multiple waves scattered from rough surfaces, to the reflections caused by the irregularities inside the materials [Hapke Bruce, 1993], and/or multiple waves diffracted on the edges. Hence, the diffusion phenomena are not favored in indoor environments comprised of only smooth surfaces, i.e., all glasses. Therefore, the present experimental method is valid for room comprised of rough surfaces (paint walls, ceilings, etc…) and/or random obstacles (tables, chairs, furniture, etc…), making the method suitable for realistic indoor environments (see Fig. 8, available in the online version).

Nevertheless, we notice from the measurements that there is no reverberation time in large open indoor environments such as halls and corridors; so the method would not be applicable in such environments.

Methodology for numerical simulations

The SEMCAD-X simulation platform is used for the simulation [SPEAG, 2009]. The same dielectric properties of the experimental procedure are used. The simulation method is shown in the lower part of the flow chart of Figure 9. In steps A1-A2, the incident LOS plane wave is determined from the measurement data by means of the Space-Alternating Generalized Expectation-Maximization Algorithm (SAGE) [Chung et al., 2002]. SAGE is an expectation-maximization based estimation algorithm used to determine the characteristics of the specular paths contained in the measurement data. In our case, we are only interested in the direction of

arrival of the LOS component since we already determined the received LOS power in the experimental procedure. Since the vertical polarization was used during the measurement, the same polarization of the incident LOS plane wave is used in the numerical simulation. In step B1 (Fig. 9), the same DMC power density determined in the experimental procedure is used and is modeled with plane waves in step B2 as follows. In the angular domain (azimuth), the DMC are assumed to have a white azimuthal spectrum [Richter, 2005], i.e., uniformly distributed over 0-2π with uniformly distributed arrival delays in time, and the elevation is assumed to be in the horizontal plane. We model the DMC power with several sets of plane waves to observe the trend of the results as we increase the number of the plane waves. Since the DMC is exponentially decaying [Andersen et al., 2007], the amplitudes of the plane waves used in the modeling follow also an exponential decay. An example (with 16 plane waves) of the DMC power modeling for the three investigated scenarios is shown in Figure 6. The damping factor of the exponential decay is the reverberation time of the room when it is empty. It is noteworthy to mention that whatever the number of plane waves used to model the DMC in a given scenario, the total incident power density is constant.

In step C (Fig. 9), the FDTD simulation of the cylinder illuminated by both the incident LOS component plus the DMC is performed. Finally, the SAR_{wb} values are retrieved in step D.

RESULTS

From the 20 time observations, we obtain 20 values of the absorption cross section of the phantom, resulting in an average value of 0.39 m^2. The LOS component and the DMC power densities values for the 3 scenarios are summarized in Table 1. The DMC power contribution

varies from 1%, 49% to 80% for scenarios 1, 2, and 3, respectively; which is in good agreement with the results in literature [Poutanen et al., 2011].

Results from experimental measurements

Using Equation (5) and Table 1, the total experimental whole-body SAR (SAR_{wb}^{exp}) are computed and listed in Table 2. In addition the DMC contribution is also shown. The DMC contribution is the ratio between the $SAR_{wb}^{\mathrm{exp},dmc}$ induced by the DMC and the total SAR_{wb}^{exp}, respectively. In the vicinity of the transmitter (scenario 1) the highest power density (697.3 mW/m^2) leads to the highest absorption rate (1284.3 µW/kg). As the phantom is moved away from the transmitter, the SAR_{wb}^{exp} decreases drastically. It can be clearly seen that the DMC effect cannot be neglected in the total absorption rate in the investigated room. Its contribution becomes more and more important for larger separations from the transmitter even though the total absorption rate is decreasing. For instance, the DMC contribution to the total absorption rate in scenario 3 is about 93%.

Results from FDTD simulations

In the following, SAR_{wb}^{fdtd} stands for the whole-body specific absorption rate from the FDTD running. ΔSAR is the relative error (in %) between the experimentally whole-body SAR and the simulated whole-body SAR and is expressed as follows:

$$\Delta SAR = \frac{\mid SAR_{wb}^{\mathrm{exp}} - SAR_{wb}^{fdtd} \mid}{SAR_{wb}^{fdtd}}$$

As explained before, the DMC is modeled with different numbers of plane waves (0, 8, 16, 32, 64 up to 81) to investigate the convergence and the accuracy of the DMC modeling.

Simulating the DMC with more than 81 plane waves was not possible, due to software and/or hardware limitations. Nevertheless, the Table 3 shows that the results do not vary much from 75 plane waves, and 81 plane waves satisfy for the DMC modeling. The absorption rate induced by *only* the DMC is also determined from numerical simulations ($SAR_{wb}^{fdtd,dmc}$).

The first scenario corresponds to a separation of 0.60 meter between the transmitter and the phantom. The LOS incident power density is about 99% of the total power, the remainder is the DMC incident power. Experimental absorption rate is about 1284.3 µW/kg, while the simulated one is 723.5 µW/kg, resulting in a relative error of 77.5% (Table 3). The second scenario corresponds to a separation of 6 meter between the transmitter and the phantom, leading to a total incident power density of 4.30 mW/m². The LOS incident power density is about 51% of the total power, while the diffuse incident power represents 49% of the total power. The experimental and simulated absorption rate values are 16.10 µW/kg and 15.48 µW/kg, respectively, leading to a relative error of about 4% (Table 3). The third scenario corresponds to a separation of 10.20 meter of the phantom from the transmitter, leading to a total incident power density of 2 mW/m². The LOS incident power density is about 20% of the total power; the remainder of 80% is the DMC incident power density. Only a relative error of about 0.71% (Table 3) is obtained between the experimental absorption rate (9.90 µW/kg) and the simulated absorption rate (9.83 µW/kg).

From the Tables 2 and 3, a maximum relative error of about 5.1%, 5.0% and 5.0% are obtained between the experimental and the simulated whole-body SAR induced by *only* the DMC ($SAR_{wb}^{exp,dmc}$ and $SAR_{wb}^{fdtd,dmc}$) for the 3 scenarios, respectively. Therefore, the high error in the first scenario is certainly due to the influence of the LOS component, showing that the method is not applicable in the near field of the antenna.

Application to real human

This section aims to determine experimentally the whole-body SAR for real humans in the office environment of Figure 8 (available in the online version). An average absorption cross section of 0.36 m^2 was obtained in Bamba et al. [2012] for real humans in the same environment (13 adults). We will use this result with the power densities derived experimentally at 2.8 GHz in the present paper to assess the whole-body SAR in a real human. Assuming a LOS component illumination from the back, or from the front of the human, we use a ratio of 2 (instead of π for a cylindrical phantom in Equation (4)) between the human ACS derived in diffuse fields and the one resulting in a LOS component illumination. Using therefore Equation (5) suitably, we obtain a real human (weight = 70 kg) whole-body SAR of 1.80 mW/kg, 16.46 µW/kg, and 9.26 µW/kg for the scenarios 1, 2, and 3, respectively. These values differ from the results obtained with canonical phantoms because of different shapes (geometry, ACS), and different weights. Instead of using normalized power density, note that we have used the actual values of the power densities (DMC and LOS component). The methodology for the assessment of the SAR$_{wb}$ in real circumstance is proposed, validated and we show in this section how it can be applied to actual human beings and we provided even real measured results.

The ratio of 2 that has been used in this section means that a person whole body surface is the sum of the body surface from the front view and the body surface from the back view, which are supposed to be equal. The ratio is a rough approximation, and its value will obviously depend on the incident LOS plane wave azimuthal angle. Therefore, future studies will be conducted to investigate this issue for all possible azimuths of the plane wave (not only front or back

illumination). The detailed application to human beings in real life is part of future research and not of this paper.

DISCUSSIONS

We validated an entirely new method to assess experimentally the whole-body SAR in a real indoor environment. Excellent agreement is obtained in the far field (scenarios 2 and 3). When assessing the whole-body SAR induced by only the DMC (comparing the experimental and numerical approach), it turns out that the presented method gives excellent results since a relative error of about 5% is obtained regardless of the investigated scenarios. This indicates that the larger error in scenario 1 for the whole-body SAR (induced by both sources) is due to the LOS component. The reason could be the fact that the absorption cross section assessment for the LOS component illumination is based on a plane wave assumption (see above), which is not ensured in the near field of the transmitter (scenario 1), especially when the receiver is not an antenna, but a phantom with large dimensions. This may explain the difference between the experimental and simulated results for the first scenario since the LOS component is dominant. Moreover, the most dominant factor influencing the whole-body SAR in the GHz region is the surface area of the human or phantom (and in turn its ACS) [Hirata et al., 2007].

The method is presented here with canonical models for validation purposes but it is primarily proposed for real humans, or for any other phantoms. For averaging and simplification sake, one can assume the same absorption cross section of humans in the methodology. However, when considering humans with different ACS, the method can be applied under 2 conditions: first, perform the measurement for only one unknown subject i.e., unknown ACS, (if there are already persons in the room their ACS should be known to assess accurately the ACS of the new subject)

and second, perform several measurement observations (for averaging purposes) to accurately assess the absorption cross section of the person.

The body mass index (BMI) is a main characteristic of human's morphology and it is evidenced that the highest (respectively lowest) BMI fits with the lowest (respectively highest) whole-body averaged SAR [Conil et al., 2008]. The human's morphology variability is studied in Conil et al. [2008], where it is shown that the BMI variability for six adult models (Visible Human, Norman, Korean, Zubal, Japan Male, and Japan Female) leads to a standard deviation of only 18%. Therefore, even though the morphology variability would affect the whole-body SAR, our simple method will lead to a reasonable value given the low variability in human's morphology.

Another important issue to address is the usefulness or validity of the use of water in the measurements/simulations instead of a tissue equivalent liquid. In general, the reader's interest increases when the SAR values are determined from actual human tissues. However, the present paper does not aim to determine the actual SAR values in human tissues; it rather validates a methodology to determine the SAR values in humans. Therefore, the methodology should not depend on a specific human tissue. It is also worthy to mention that we are not dealing with the localized SAR, but rather the whole-body SAR. Hirata et al. [2007] showed that the most dominant factor influencing the whole-body SAR in the GHz region is the surface area of the human, and not the tissues properties.

We already applied the method validated in this paper to actual human people [Bamba et al. 2012], consisting of real tissues, which are more realistic tissues than the tissue equivalent liquid. We chose to use water to be clear on the purpose of this paper: this is a validation of a methodology and the values cannot be used as actual absorptions. Moreover, the equivalent

tissue liquids are "worse-case" tissues according to the International Electrotechnical Commission (IEC) standard 62209 [IEC, 2005], not realistic and not relevant to determine actual absorptions.

Finally, we simulated in FDTD the whole-body SAR for the considered scenarios with muscle (ε_r = 52.302 and σ = 1.9887 S/m) and skinwet (ε_r = 42.375 and σ = 1.8129 S/m) to show that our results will not vary significantly compared to the SAR_{wb} derived from these tissues properties. The dielectric properties of the muscle and the skinwet can be found in the Institute for Applied Physics [IFAC] data base. The DMC has been modeled with 81 plane waves surrounding the phantom, similarly to the previous modeling. For each scenario, ΔSAR is the relative error between simulated-water and simulated-tissue based results.

As it can be seen in Table 4, a maximum deviation of about 21 % between the water based simulated SAR and the tissues-based simulated SAR. This maximum deviation occurs for liquid simulating the skin, whereas the minimum deviation of about 14 % occurs for the liquid simulating the muscle. The "ND" in Table 4 stands for "Not-Defined". This simulation shows that the water based whole-body SAR simulation values are representative of the skinwet and muscle based SAR_{wb} values at 2.8 GHz.

CONCLUSIONS

A method to assess experimentally the whole-body average specific absorption rate in a complex indoor environment is validated through numerical simulations. The method is applicable for any phantom or actual human. Different scenarios are investigated to ensure the validity of the method at different locations within the investigated room. The experimental and numerical results agree very well as long as the plane wave assumption is valid (not in the vicinity of the

transmitter), the relative errors for the 3 investigated scenarios are 77.5%, 4.0% and 0.71%, respectively. The validation is worthy because it has showed the validity domain of the method: the method is only applicable in the far field of the transmitting antenna.

The diffuse multipath components contribution in the whole-body specific absorption rate is also studied in this paper. The average specific absorption rate decreases with increasing separation from the transmitter. The larger the separation is, the larger will be the contribution of the DMC in the induced whole-body specific absorption rate.

In our future work, the correlation between the absorption cross section and the polarization of the incident LOS plane wave will be investigated (via FDTD simulations). Hence the method will be applied for different polarizations of the LOS component and can also be extended to the other specular paths (not only the LOS component).

REFERENCES

Andersen JB, Nielsen JØ, Pedersen GF, Bauch G, Herdin M. 2007. Room Electromagnetics. IEEE Antennas and Propagation Magazine 49(2): 27-33.

Andersen JB, Chee KL, Jacob M, Pedersen GF, Kürner T. 2012. Reverberation and Absorption in an Aircraft Cabin with the Impact of Passengers. IEEE Antennas and Propagation Transactions 60(5): 2472-2480.

Bamba A, Joseph W, Andersen JB, Tanghe E, Vermeeren G, Plets D, Nielsen J Ø, Martens L. 2012. Experimental Assessment of Specific Absorption Rate Using Room Electromagnetics. IEEE Transactions on Electromagnetic Compatibility (IEEE EARLY ACCESS ARTICLE), http://ieeexplore.ieee.org/stamp/stamp.jsp?arnumber=06174464 (accessed on July 10, 2012).

Bernardi P, Cavagnaro M, Cicchetti R, Pisa S, Piuzzi E, Testa O. 2003. A UTD/FDTD Investigation on Procedures to Assess Compliance of Cellular Base-Station Antennas With Human-Exposure Limits in a Realistic Urban Environment. IEEE Transactions on Microwave Theory and Techniques 51: 2409-2417.

Bürgi A, Frei P, Theis G, Mohler E, Braun-Fahrländer C, Fröhlich J, Neubauer G, Egger M, Röösli M. 2010. A model for Radiofrequency Electromagnetic Field Predictions at Outdoor and Indoor Locations in the Context of Epidemiological Research. Bioelectromagnetics 31: 226-236.

Chung JP, Böhme JF. 2002. DOA estimation using fast EM and SAGE algorithms. Signals Processing 82: 1753-1762.

Conil E, Hadjem A, Lacroux F, Wong MF, Wiart J. 2008. Variability analysis of SAR from 20 MHz to 2.4 GHz for different adult and child models using finite-difference time-domain. Physics In Medicine And Biology 53: 1511-1525.

Dimbylow PJ. 2002. Fine resolution calculations of SAR in the human body for frequencies up to 3 GHz. Physics in Medicine and Biology 47: 2835-2846.

Friis HT. 1946. A note on a Simple Transmission Formula. Proceedings of the IRE and Waves and Electrons 34(5): 254-256.

Hapke Bruce. 1993. Theory of Reflectance and Emittance Spectroscopy. The Press Syndicate of the University of Cambridge. Cambridge, United Kingdom.

Hirata A, Kodera S, Wang J, Fujiwara A. 2007. Dominant Factors Influencing Whole-Body Average SAR Due to Far-Field Exposure in Whole-Body Resonance Frequency and GHz Regions. Bioelectromagnetics 28: 484-487.

ICNIRP - International Commission on Non-Ionizing Radiation Protection (ICNIRP). 1998. Guidelines for limiting exposure to time-varying electric, magnetic, and electromagnetic fields (up to 300 GHz). Health Physics 74(4): 494-522.

IEC - International Electrotechnical Commission. 2005. Human Exposure To Radio Frequency Fields From Hand-held And Body-mounted Wireless Communication Devices Human Models, Instrumentation, and procedures To Determine The Specific Absorption Rate (SAR) for Hand-held Devices Used In The Close Proximity To The Ear (Frequency Range Of 300 MHz To 3 GHz). International Standard 62 209.

IFAC - Institute for applied Physics. An internet resource for the calculation of the Dielectric Properties of Body Tissues in the frequency range 10 Hz - 100 GHz, http://niremf.ifac.cnr.it/tissprop/ (accessed on July 10, 2012). Florence, Italy.

Joseph W, Martens L. 2005. Comparison of Safety Distances Based on the Electromagnetic Field and Based on the SAR for Occupational Exposure of a 900-MHz Base Station Antenna. IEEE Transactions on Electromagnetic Compatibility 47(4): 977-985.

Joseph W, Vermeeren G, Verloock L, Martens L. 2010. Estimation of Whole-Body SAR From Electromagnetic fields Using Personal Exposure Meters. Bioelectromagnetics 31: 286-295.

Kühn S, Jennings W, Christ A, Kuster N. 2009. Assessment of induced radio-frequency electromagnetic fields in various anatomical human. Physics in Medicine and Biology 54: 875-890.

Merewether DE, Fisher R, Smith FW. 1980. On implementing a numeric Huygen's source scheme in a finite difference program to illustrate scattering bodies. IEEE Transactions on Nuclear Science 27(6): 1829-1833.

Poutanen J, Salmi J, Haneda K, Kolmonen VM, Vainikainen P. 2011. Angular and Shadowing Characteristics of Dense Multipath Components in Indoor Radio Channels. IEEE Transactions on Antennas and Propagation 59: 245-253.

Richter A. 2005. Estimation of Radio Channel Parameters: Models and Algorithms. PhD thesis. Faculty of Electrical Engineering and Information Technology at the Technical University. Ilmenau, Germany.

SPEAG 2009. SEMCAD X *Reference Manual* Schmid & Partner Engineering AG, www.semcad.com (accessed on March 20, 2012). Zürich, Switzerland.

Taflove A, Hagness S. 2005. Computational Electrodynamics: The Finite-Difference Time-Domain Method 3rd edn. Norwood, MA: Artech House Publishers

Vermeeren G, Joseph W, Christof O, Martens L. 2008. Statistical Multipath Exposure of a Human in a Realistic Electromagnetic Environment. Health Physics 94(4): 345-354

Wang J, Fujiwara O, Kodera S, Watanabe S. 2006. FDTD calculation of whole-body average SAR in adult and child models for frequencies from 30 MHz to 3 GHz. Physics in Medicine and Biology 51: 4119-4127.

LIST OF TABLES

LIST OF FIGURES

	Distance phantom-Tx (m)	Line Of Sight (LOS) power density (mW/m^2)	Diffuse Multipath Components (DMC) power density (mW/m^2)	Total power density (mW/m^2)
Scenario 1	0.60	694.40 (99%)	2.90 (1%)	697.30
Scenario 2	6.00	2.20 (51%)	2.10 (49%)	4.30
Scenario 3	10.20	0.40 (20%)	1.60 (80%)	2.00

	Scenario 1	Scenario 2	Scenario 3
SAR_{wb}^{exp} (µW/kg)	1284.30	16.10	9.90
$SAR_{wb}^{\mathrm{exp},dmc}$ (µW/kg)	16.63	12.04	9.18
Part of the DMC in the SAR_{wb}^{exp}	1.3%	75%	92.72%

	DMC(no. of plane waves)	0	8	16	32	64	75	78	80	81
Scenario 1	SAR_{wb}^{fdtd} (μW/kg)	668	717	705.3	707.4	717.8	721.5	722.5	723.2	**723.5**
	$SAR_{wb}^{fdtd,dmc}$ (μW/kg)	0	3.6	3.32	6.32	12.52	14.67	15.25	15.64	**15.83**
	Part of DMC in the SAR_{wb}^{fdtd} (%)	0	0.5	0.47	0.89	1.74	2.03	2.11	2.16	**2.19**
	Percentage error (ΔSAR)	92.26	79.12	82.09	81.55	78.92	78	77.75	77.58	**77.5**
Scenario 2	SAR_{wb}^{fdtd} (μW/kg)	2.12	6.90	6.15	8.30	13.00	14.60	15.04	15.34	**15.48**
	$SAR_{wb}^{fdtd,dmc}$ (μW/kg)	0	2.60	2.40	4.57	9.07	10.62	11.04	11.33	**11.47**
	Part of DMC in the SAR_{wb}^{fdtd} (%)	0	37.70	39.02	55.06	69.77	72.74	73.40	73.86	**74.09**
	Percentage error (ΔSAR)	659	133.3	161.7	93.97	23.84	10.27	7.04	4.95	**4.00**
Scenario 3	SAR_{wb}^{fdtd} (μW/kg)	0.38	3.18	2.82	4.46	7.96	9.17	9.50	9.72	**9.83**
	$SAR_{wb}^{fdtd,dmc}$ (μW/kg)	0	1.98	1.83	3.48	6.91	8.09	8.41	8.63	**8.74**
	Part of DMC in the SAR_{wb}^{fdtd} (%)	0	62.26	64.89	78.03	86.81	88.22	88.53	88.79	**88.91**
	Percentage error (ΔSAR)	2505	211	251	121	24.37	7.96	4.21	1.85	**0.71**

			Water		Skin Wet		Muscle	
			LOS	LOS+DMC	LOS	LOS+DMC	LOS	LOS+DMC
Scenario 1		SAR$_{wb}$ (µW/kg)	668	723.5	846.88	916.33	780.25	844.55
		ΔSAR (%)	ND	ND	21.12	21.04	14.38	14.33
			LOS	LOS+DMC	LOS	LOS+DMC	LOS	LOS+DMC
Scenario 2		SAR$_{wb}$ (µW/kg)	2.12	15.76	2.68	19.45	2.47	17.98
		ΔSAR (%)	ND	ND	20.98	20.41	14.23	13.92
			LOS	LOS+DMC	LOS	LOS+DMC	LOS	LOS+DMC
Scenario 3		SAR$_{wb}$ (µW/kg)	0.38	9.83	0.4888	12.34	0.45	11.41
		ΔSAR (%)	ND	ND	22.10	20.34	15.45	13.87
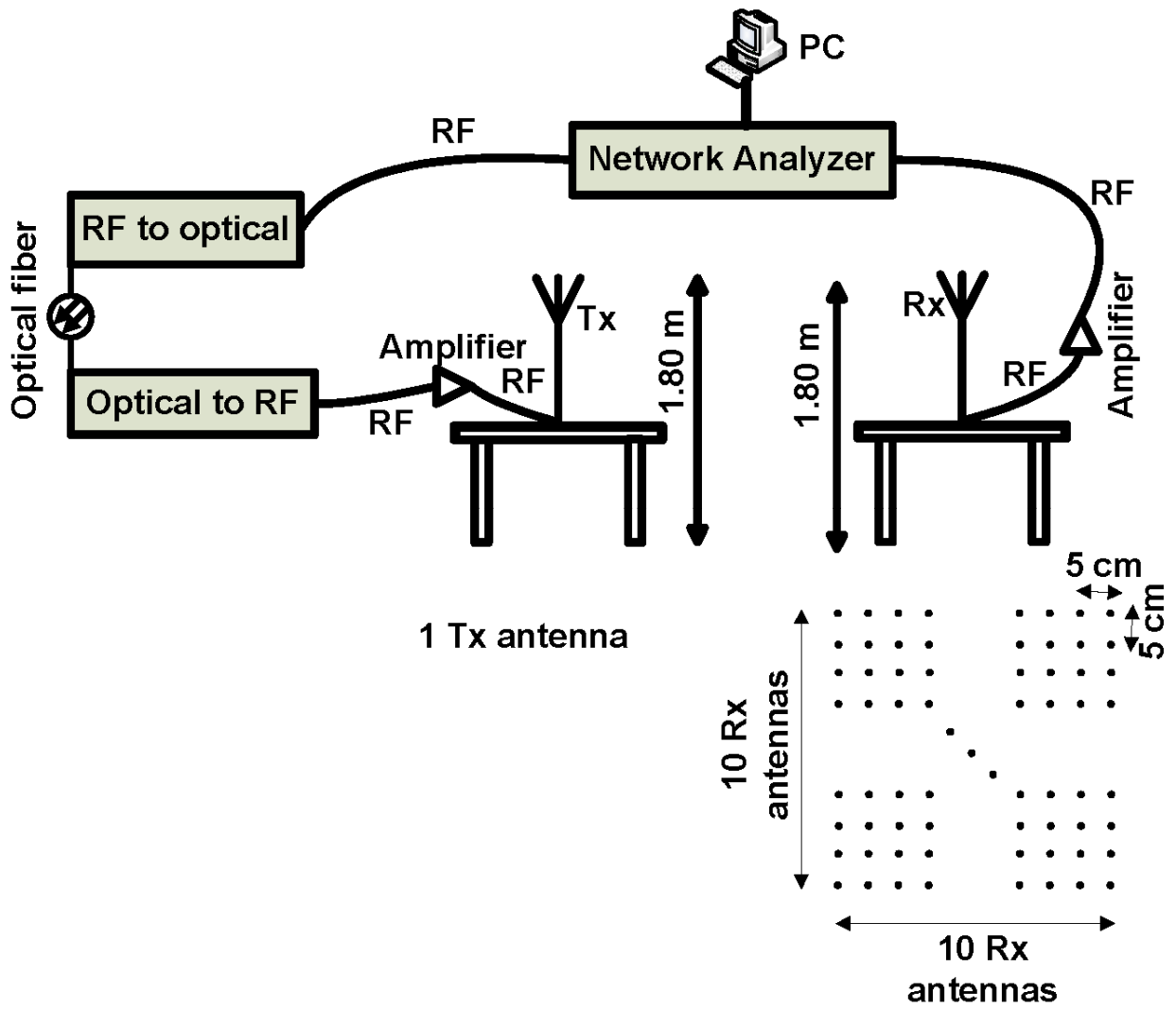
Figure 1: The virtual MIMO system
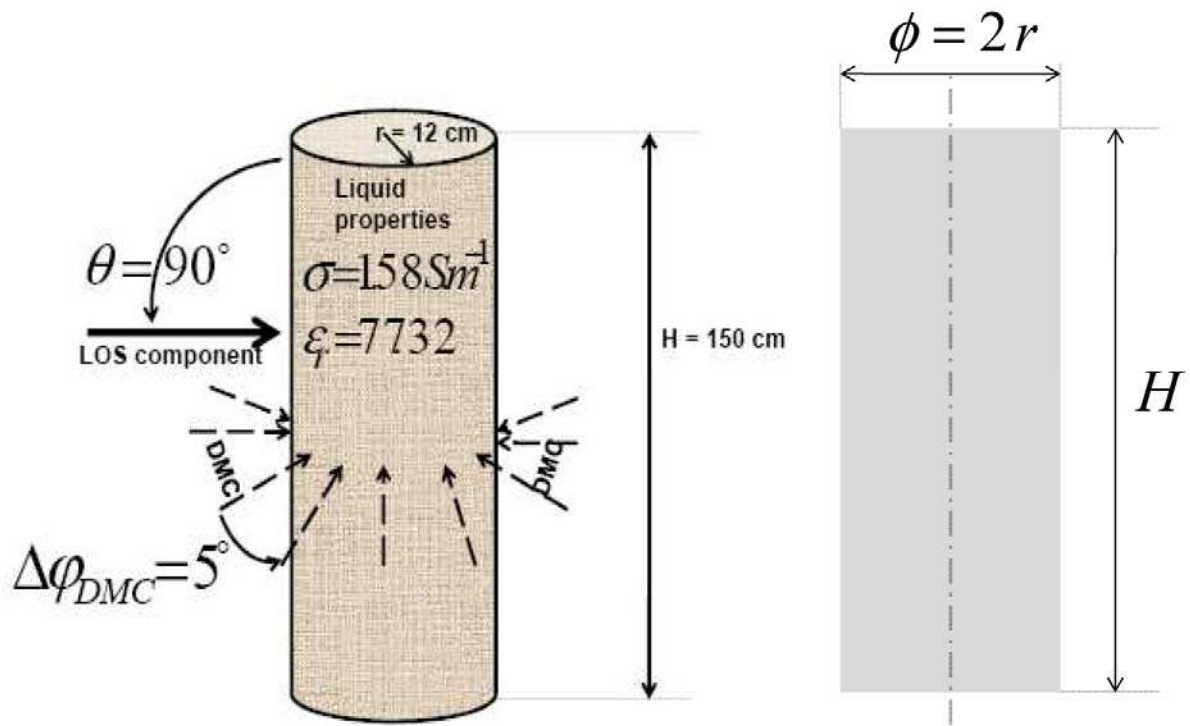
Figure 2: A Phantom plus the involved powers and the front view (by a plane wave)
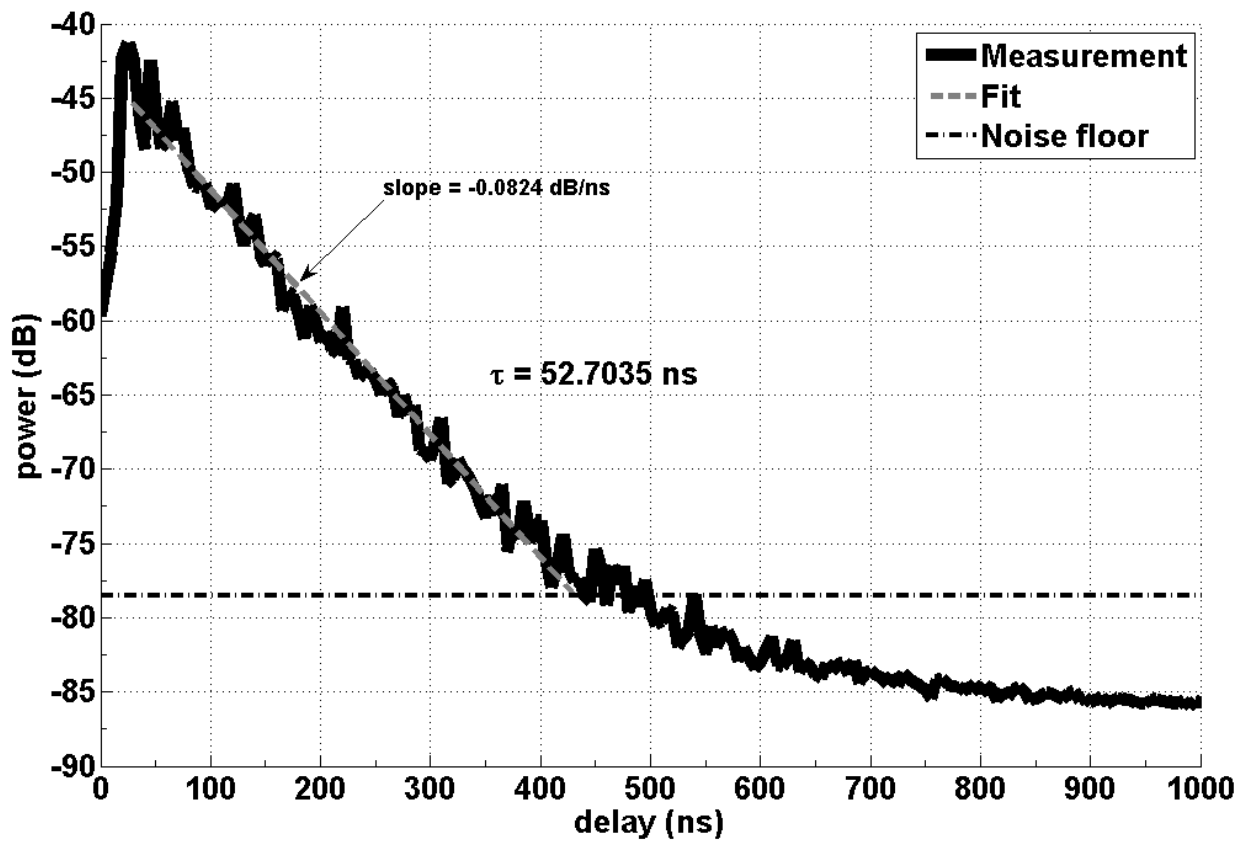
Figure 3: A PDP with the corresponding reverberation time
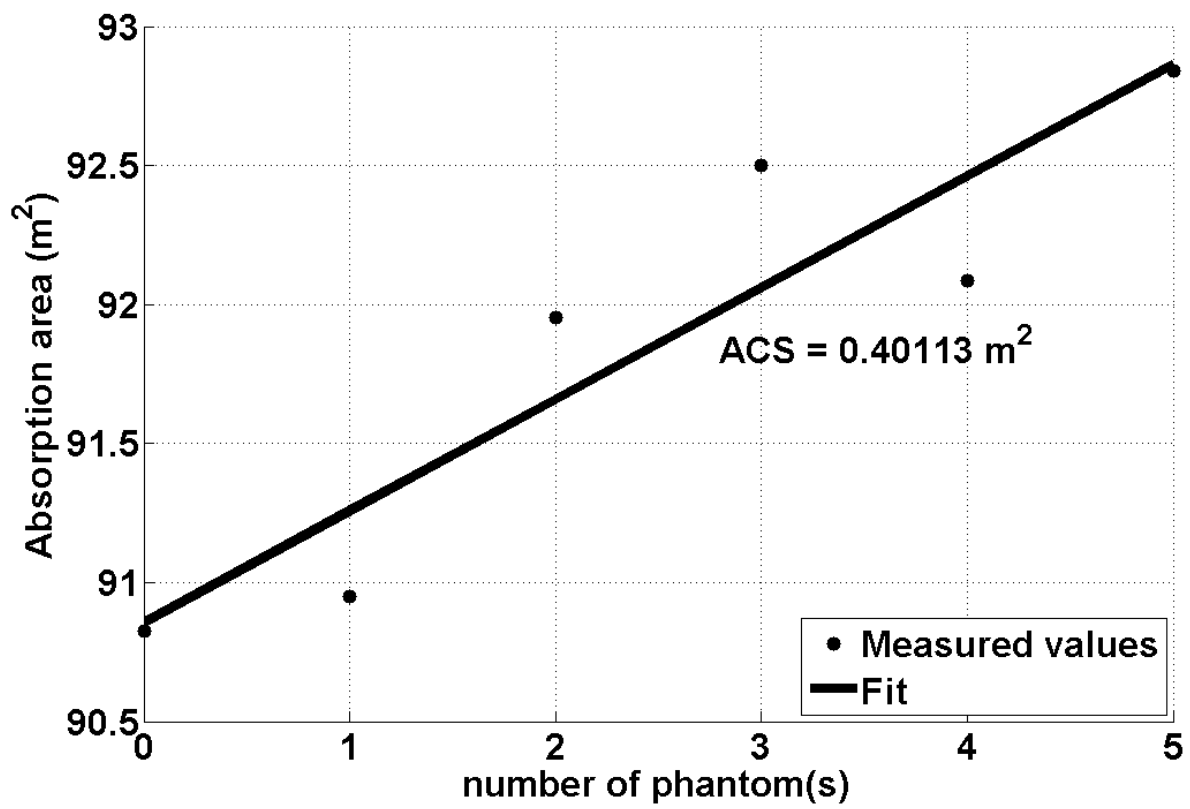
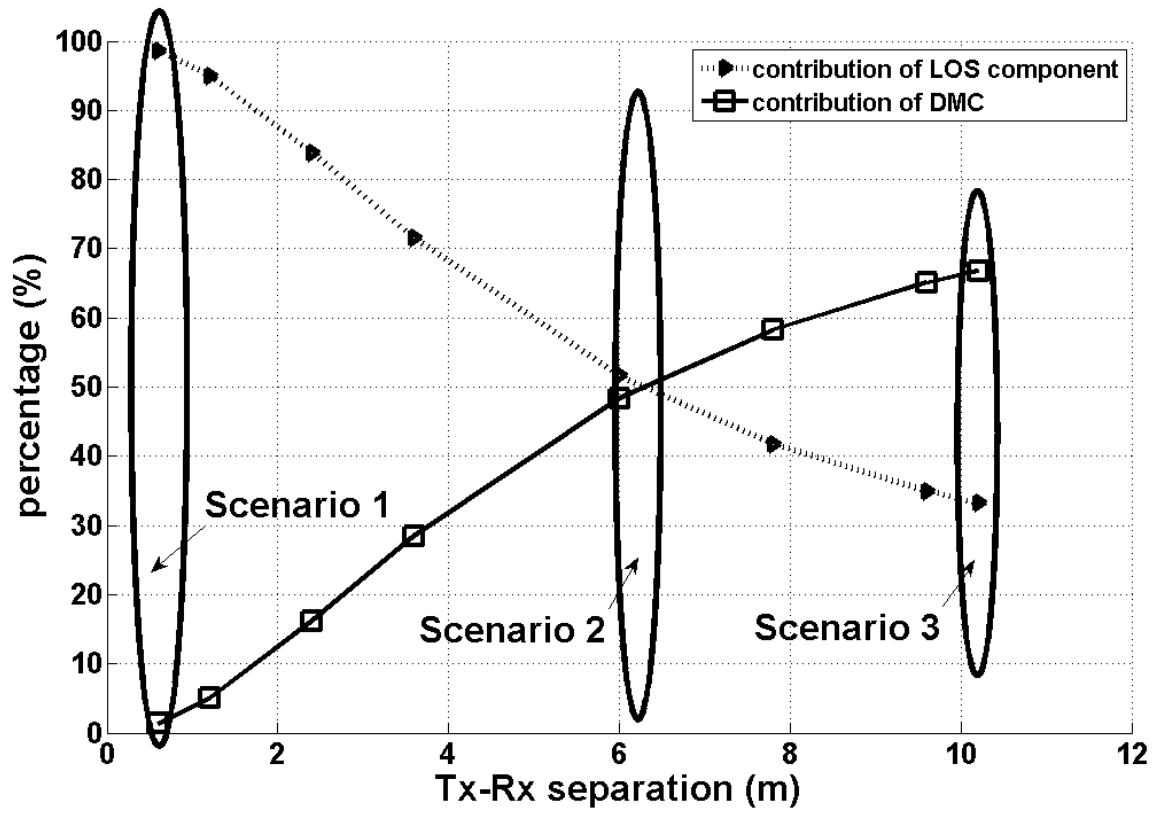**Figure 4: An example of the absorption cross section (for one time observation)**

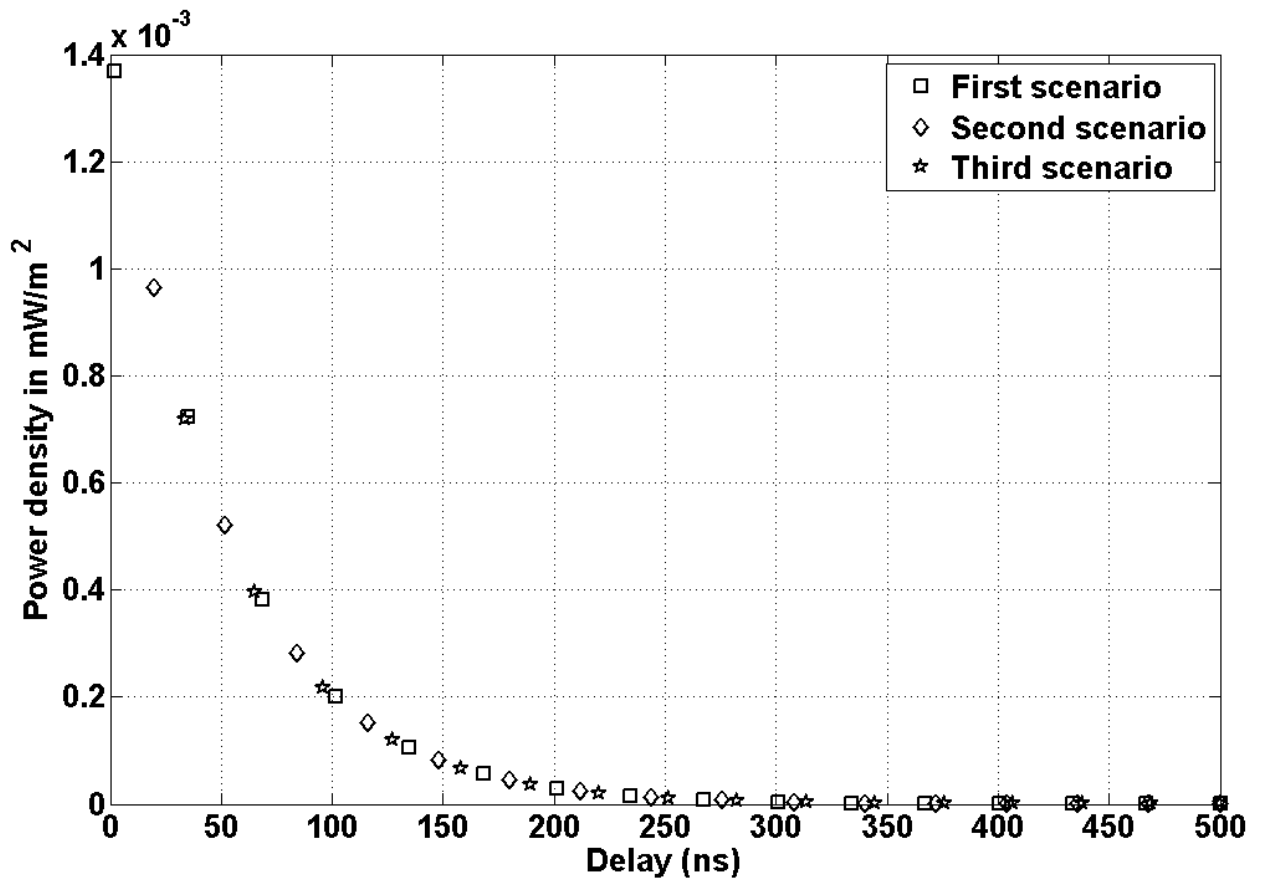Figure 5: Contribution of the DMC and the LOS component in the total power density

Figure 6: Modeling of the DMC power density (with 16 plane waves for instance) for the 3 scenarios